Additive manufacturing of patterned 2D semiconductor through recyclable masked growth

Yunfan Guo[a], Pin-Chun Shen[a], Cong Su[b], Ang-Yu Lu[a], Marek Hempel[a], Yimo Han[c], Qingqing Ji[a], Yuxuan Lin[a], Enzheng Shi[d], Elaine McVay[a], Letian Dou[d], David A. Muller[c], Tomás Palacios[a], Ju Li[b], Xi Ling[e,f,g,1], and Jing Kong[a,1]

[a]Department of Electrical Engineering and Computer Science, Massachusetts Institute of Technology, Cambridge, MA 02139; [b]Department of Nuclear and Materials Science and Engineering, Massachusetts Institute of Technology, Cambridge, MA 02139; [c]School of Applied & Engineering Physics, Cornell University, Ithaca, NY 14850; [d]Davidson School of Chemical Engineering, Purdue University, West Lafayette, IN 47907; [e]Department of Chemistry, Boston University, Boston, MA 02215; [f]Division of Materials Science and Engineering, Boston University, Boston, MA 02215; and [g]The Photonics Center, Boston University, Boston, MA 02215

The 2D van der Waals crystals have shown great promise as potential future electronic materials due to their atomically thin and smooth nature, highly tailorable electronic structure, and mass production compatibility through chemical synthesis. Electronic devices, such as field effect transistors (FETs), from these materials require patterning and fabrication into desired structures. Specifically, the scale up and future development of "2D"-based electronics will inevitably require large numbers of fabrication steps in the patterning of 2D semiconductors, such as transition metal dichalcogenides (TMDs). This is currently carried out via multiple steps of lithography, etching, and transfer. As 2D devices become more complex (e.g., numerous 2D materials, more layers, specific shapes, etc.), the patterning steps can become economically costly and time consuming. Here, we developed a method to directly synthesize a 2D semiconductor, monolayer molybdenum disulfide (MoS_2), in arbitrary patterns on insulating SiO_2/Si via seed-promoted chemical vapor deposition (CVD) and substrate engineering. This method shows the potential of using the prepatterned substrates as a master template for the repeated growth of monolayer MoS_2 patterns. Our technique currently produces arbitrary monolayer MoS_2 patterns at a spatial resolution of 2 μm with excellent homogeneity and transistor performance (room temperature electron mobility of 30 cm^2 V^{-1} s^{-1} and on–off current ratio of 10^7). Extending this patterning method to other 2D materials can provide a facile method for the repeatable direct synthesis of 2D materials for future electronics and optoelectronics.

2D semiconductor | monolayer MoS_2 | patterned growth | growth mechanism | recyclable masked growth

In recent years, the family of monolayer transition metal dichalcogenides (TMDs) has become attractive semiconducting crystals for nano- and flexible electronics due to their atomic thinness, high carrier mobility, and excellent flexibility (1, 2). In addition, TMDs have drawn considerable attention in condensed matter due to the unique electronic band structures and intriguing valley–spin coupling, making them promising for valleytronics (3), piezoelectrics (4), bandgap modulation (5), and high-quantum efficiency optical/optoelectronic applications (6, 7).

To fabricate future 2D-based electronics and optoelectronics structures, it is necessary to pattern 2D materials for contacts, gating, optical access, etc. (8, 9). At present, patterning TMDs have relied on either subtractive or additive manufacturing. "Growth and etch" (10–12) is perhaps the most typical method of 2D patterning, where it utilizes subtractive manufacturing (akin to "top down") to lithographically define and subsequently etch away unwanted areas of 2D material. This method has spatial resolution roughly down to nanometers (when using electron beam lithography), but it has a high manufacturing cost and can become time consuming. Additionally, the inevitable generation of multiple layers (which is necessary when constructing an integrated system) becomes difficult to handle, as selective etching of 2D materials still poses fabrication

challenge (also due to their atomic thinness). Furthermore, contaminations between interfaces and rough, amorphous edge terminations may be introduced during fabrication, thus increasing the chance for quality deterioration of as-grown materials. To avoid surface contamination by resist residues, shadow mask (13) and laser cutting (14) can be considered, but the poor spatial resolutions typically are in the range of near millimeters to hundreds of micrometers.

However, for additive manufacturing ("bottom-up") techniques, inkjet printing (15) has been extensively used for the large-scale preparation of TMD patterns. Nevertheless, it requires solution-based 2D flakes (typically multilayered), and the minimal feature size is usually larger than 10 μm. Various efforts have been devoted to prepattern seed precursors [molybdenum oxide (MoO_3), ammonium heptamolybdate (16), or Au catalyst (17)] to generate patterned TMD structures directly, although preventing multilayer islands growing on monolayer regions still turned out to be challenging. Substrate modification by O_2 plasma provides a simpler route to patterned TMDs (18, 19), but the reported electrical mobility has been two orders of magnitude lower than as-grown TMDs (1 cm^2 V^{-1} s^{-1}) with poor spatial resolution (~100 μm).

Significance

Traditional semiconductor fabrication methods, such as lithography and etching, have been sufficient for the needs of integrated circuits over past decades. Their applicability has also been demonstrated in emerging 2D materials, which offers facile processing over large lateral dimensions, while unique and remarkable properties due to the confinement within atomic thicknesses. Nevertheless, each fabrication step adds cost to the manufacturing and increases the possibility of quality degradation. Here, we developed a method to directly synthesize arbitrary monolayer molybdenum disulfide patterns with high spatial resolution, excellent homogeneity, and electrical performance on insulating SiO_2/Si. Significantly, our on-demand method allows for the repeated growth of patterned 2D materials with preserved structural integrity and material qualities, paving the way for simpler and cost-effective fabrication.

ENGINEERING

Herein, through in-depth studies of the growth mechanism and precursor control, we have found that plasma-based substrate modification can be used to directly grow patterned monolayer molybdenum disulfide (MoS$_2$) with high crystal quality, diverse geometries, high spatial resolution (2 μm at present, limited by laser lithography), and high electrical mobility (~30 cm^2 V^{-1} s^{-1}) on SiO$_2$/Si substrate. The same patterning mask can be recycled for repeated growth with consistent material morphology and quality each time, which demonstrates the potential of this method for a "master–replica" type of repeated manufacturing. Such an additive manufacturing method opens up the possibilities for wide applications of 2D TMD nanostructures in modern electronics and optoelectronics with much simpler fabrication.

Results and Discussions

Substrate modification is the first step to achieve the patterned MoS$_2$ structures as shown in Fig. 1A. As a proof of concept, we have chosen to define MoS$_2$ in the shape of kirigami patterns. Traditionally, kirigami is a technique to create 3D structures from 2D sheets and has been applied in 2D materials to build robust macro- or microscale structures with tunable mechanical properties (20–22). Photolithography defines patterns of photoresist on the substrates (*SI Appendix*, Fig. S1) while undeveloped areas are etched away using O$_2$ plasma, which simultaneously modifies the surface of SiO$_2$ substrate. After removing the developed photoresist, MoS$_2$ can selectively grow on plasma-treated areas, similar to our previous studies (details are in *Methods*) (23, 24). As the plasma treatment creates a region with higher surface energy and enhanced hydrophilicity (discussion below), the hydrophilic salt perylene-3,4,9,10-tetracarboxylic acid tetrapotassium

(PTAS) is used to promote seeded, selective MoS$_2$ growth only at the O$_2$ plasma-treated areas, forming as-grown patterned MoS$_2$.

Inspection of the resultant growth using optical microscopy (OM) clearly shows a patterned growth of MoS$_2$ (in the shape of a wave array) on SiO$_2$/Si (Fig. 1B). The reflectance contrast of the green-tinted MoS$_2$, which comprises the wave, is uniform, with a strap width of 20 μm (tunable by changing the patterns on the substrate). Fig. 1C shows that MoS$_2$ grows at opposite locations (in contrast to Fig. 1B) when a negative photoresist was used for the same pattern. Through this technique, monolayer MoS$_2$ patterns with diverse morphologies and different feature sizes can be obtained by only changing the original growth "mask" (*SI Appendix, Fig. S2 A1–C2*). Currently, the minimal spatial resolution is 2 μm, which is limited by the direct laser writing instrument (*SI Appendix, Fig. S2 D1 and D2*). To evaluate the surface morphology of the MoS$_2$ patterns, we use atomic force microscopy (AFM). We first observed that the strong O$_2$ plasma etching causes a height difference between the pristine SiO$_2$ regions and the etched regions of about 2 nm (*SI Appendix, Fig. S3A*). After the growth of MoS$_2$, a flat and pristine monolayer fills in the recessed region (Fig. 1D) and reduces the height difference to ~1.3 nm (*SI Appendix, Fig. S3B*), confirming that the thickness of MoS$_2$ patterns is monolayer (~0.7 nm).

To evaluate the crystallinity of the monolayer MoS$_2$ patterns, characterizations with photoluminescence (PL) and Raman spectroscopy were carried out. A strong PL emission at around 1.85 eV with an FWHM intensity of about 60 meV was observed on all tested samples, consistent with the emission of grown monolayer MoS$_2$ (Fig. 1G) (25). For Raman spectroscopy, the frequency difference between Raman peaks located at 383 cm^{-1}
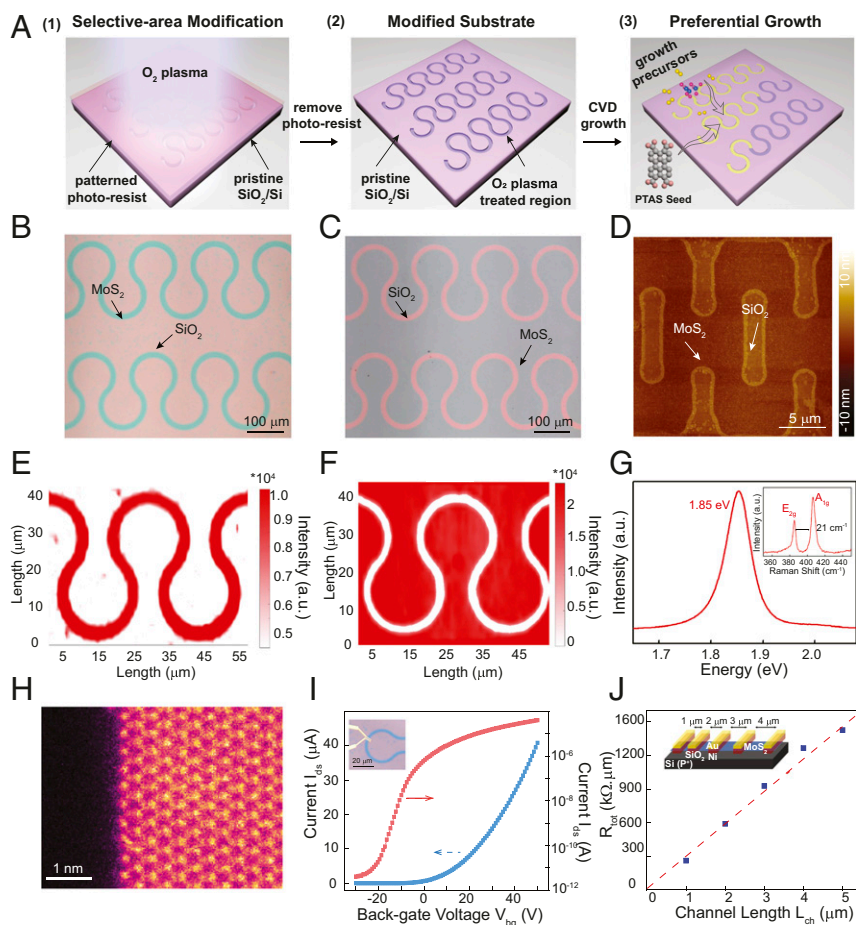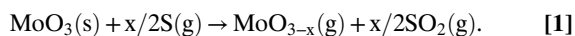

Fig. 1. Patterned growth and characterization of MoS$_2$ nanostructures. (*A*) Schematic representation of the procedures for the direct growth of MoS$_2$ nanostructures via seed-promoted growth and substrate engineering. Step 1: the selective-area modification process by lithography patterning and O$_2$ plasma etching; step 2: the patterned regions are distinguished from pristine SiO$_2$/Si substrates after modification; step 3: the preferential growth of MoS$_2$ on patterned SiO$_2$/Si regions. (*B*) A typical OM image of a monolayer MoS$_2$ wave array. (*C*) OM image of a monolayer MoS$_2$ wave film that grows at the opposite locations when a negative photoresist was used for the wave pattern in *B*. (*D*) AFM image of a monolayer MoS$_2$ kirigami structure showing the flat surface and ordered edge morphology. (*E* and *F*) PL mappings for monolayer MoS$_2$ wave arrays and the inversed wave film pattern. (*G*) A typical PL spectrum collected on the monolayer MoS$_2$ wave structures. (*Inset*) A typical Raman spectrum collected on the monolayer MoS$_2$ wave structures. (*H*) ADF-STEM image of a patterned monolayer MoS$_2$ edge showing the clean and ordered edge at atomic scale. (*I*) Transfer ($I_{ds} - V_{bg}$) characteristic of a typical back-gated transistor fabricated on our CVD-patterned MoS$_2$ film with gate voltages from −30 to 50 V and a bias V_{ds} fixed at 1 V. The room temperature electron mobility of the transistor is 29.3 cm^2 V^{-1} s^{-1}. The red curve shows the transfer characteristic of the same MoS$_2$ transistor in logarithmic scale. The on–off current ratio is ~10^7. (*Inset*) Optical image of a typical MoS$_2$ device based on the wave pattern. (*J*) Total device resistance R_{TOT} normalized by width vs. channel length L_{ch} measured at a carrier concentration n of ~ 1.8 × 10^{12} cm^{-2}, yielding a contact resistance of R_c ~ 6.7 kΩ·μm from the vertical intercept. (*Inset*) The schematic of our TLM devices with Ni/Au contacts.

Fig. 2. Mechanism study for the patterned growth of monolayer MoS_2 nanostructures. (*A*) Schematic illustration of the growth mechanism of the patterned growth of MoS_2. (*B*) Comparison of contact angles for pristine, Ar plasma-treated, and O_2 plasma-treated SiO_2/Si substrates. (*C*) DFT calculation for the binding energies between H_2O and SiO_2/Si substrate treated by O_2 plasma and Ar plasma. (*D*) DFT calculation for the binding energies between Mo_3O_9 and SiO_2/Si substrate treated by O_2 plasma and Ar plasma. (*E, Upper Left*) OM image of MoO_2 particles preferentially deposited on patterned SiO_2/Si regions without PTAS. (*E, Lower Left*) OM image of MoO_2 particles preferentially deposited on patterned SiO_2/Si regions with the presence of PTAS. (*E, Right*) Raman spectra collected at the regions indicted by the red, blue, and black circles in the OM images in *Left*; several MoO_2 Raman peaks are labeled in the spectra. It is shown that MoO_2 particles exhibit a clear preference to deposit on the patterned region and that the Raman peaks of MoO_2 are stronger with the presence of PTAS. (*F, Upper Left*) OM image of monolayer MoS_2 flakes grown on O_2 plasma-treated SiO_2/Si substrate with the assistance of PTAS. The domain size of MoS_2 is around 20 μm. (*F, Upper Right*) OM image of small MoS_2 flakes grown on O_2 plasma-treated SiO_2/Si substrate without PTAS. (*Inset*) AFM images of MoS_2 small flakes with domain size around 300 nm. (*F, Lower Left*) OM image of monolayer MoS_2 flakes grown on pristine SiO_2/Si substrate with the assistance of PTAS. The domain size of MoS_2 is around 8–10 μm. (*F, Lower Right*) OM image of small MoS_2 flakes grown on pristine SiO_2/Si substrate without PTAS seed. (*Inset*) AFM images of MoS_2 small flakes with domain size around 200 nm, indicating the poor quality of MoS_2 growth.

(E_{2g}) and 404 cm^{-1} (A_{1g}) is 21 cm^{-1}, further confirming that the patterned MoS_2 is monolayers as well (Fig. 1*G, Inset*). To assess the spatial homogeneity, we performed PL and Raman mappings across the grown structures. PL mappings at 670 nm in Fig. 1 *E* and *F* and *SI Appendix*, Fig. S4 *C2 and D2* confirmed that monolayer MoS_2 follows the prepared wave and rectangle kirigami patterns reasonably well with crystalline homogeneity. Additionally, Raman mappings of the E_{2g} mode (*SI Appendix*, Fig. S4 *A2, B2, C3, and D3*) and the A_{1g} mode (*SI Appendix*, Fig. S4 *A3, B3, C4, and D4*) both exhibit a high degree of spatial uniformity. All optical spectroscopy data indicate that this patterned manufacture produces high-quality MoS_2.

Through transmission electron microscopy (TEM) examination, it was found that the patterned MoS_2 maintains reasonably sharp and clean edges. *SI Appendix*, Fig. S5*A* shows a typical bright-field TEM image of an MoS_2 edge, while *SI Appendix*, Fig. S5*B* shows the corresponding dark-field TEM and diffraction pattern (*SI Appendix*, Fig. S5*B, Inset*). Through the dark-field TEM, the patterned MoS_2 can be clearly observed as polycrystalline (typical in all of these growth results) with three domains. Excluding a wrinkle likely caused by the TEM transfer process, there is no visible gap or bilayer area over the film. Particularly, the edges formed by domain merging remain flat and sharp. Compared with the growth-and-etch method, one additional advantage for this direct growth is that the as-grown edges are clean, are sharp, and exhibit fewer contaminations or atomic defects as revealed by the atomic-resolution annular dark-field scanning TEM (ADF-TEM) image (shown in Fig. 1*H*). This is imperative in preserving the intrinsic properties of TMD materials, especially for electrical performance.

In conventional nanofabrication or device manufacturing, photolithography and subsequent plasma etching are necessary to define individual devices from the continuous film, which can

degrade the performance of the devices, as photoresist residues may induce scattering centers and high contact resistances at the interface. In comparison, patterned monolayer MoS_2 at predefined positions would preserve intrinsic electronic properties and facilitate the system-level fabrication for multifunctional devices (Fig. 1*I, Inset*). To evaluate the electronic performance, we fabricated back-gated field effect transistors (FETs) on different monolayer MoS_2 patterns. Our MoS_2 FETs shows high performance based on the average electronic properties (*SI Appendix*, Fig. S6). Fig. 1*I* and *SI Appendix*, Fig. S7*A* exhibit the typical transfer ($I_{ds} - V_{bg}$) and output ($I_{ds} - V_{ds}$) characteristics, respectively, of an FET fabricated on an MoS_2 wave pattern. The MoS_2 transistor exhibits *n*-type conduction with I_{on}/I_{off} ratio up to ∼10^7. The electron mobility of our MoS_2 FET reaches 29.3 cm^2 V^{-1} s^{-1} at room temperature in air (Fig. 1*I*), which is comparable with the reported values of metal–organic chemical vapor deposition-grown samples (26). Furthermore, the contact resistance (R_c) of our MoS_2 FETs was further extracted based on the transfer length method (TLM). Fig. 1*J* shows a linear fit to the total resistance normalized by channel width (R_{TOT}) vs. channel length (L_{ch}). We extract R_c ∼ 6.7 kΩ·μm at room temperature for a carrier density *n* of about 1.8×10^{12} cm^{-2}. This contact resistance is consistent with previous reported values of Ni-contacted MoS_2 devices on exfoliated samples (27). Significantly, one of the crucial factors to achieve a low contact resistance is the clean interface between MoS_2 and metal electrodes, which is attained through the direct growth of MoS_2 patterns.

Understanding the growth mechanism is critical to obtaining reliable predefined MoS_2 patterns via such direct growth paradigm. To this end, we systematically investigated the substrate modification, seed-promoted nucleation, and the effect of the sulfur vapor on the growth process. A generic mechanism of thin film growth considers chemical potentials and surface energies of
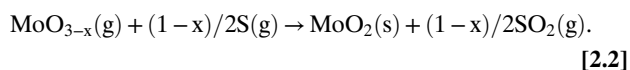
epitaxial layers and the substrates (28). Therefore, increasing the surface energy on selective areas of the substrate favors patterned monolayer growth over the growth of multilayer particles. As shown in Fig. 2A, after patterning and O₂ plasma treatment, the SiO₂/Si substrate was composed of modified regions and pristine regions. We compared the contact angles for each type of surface in Fig. 2B. The contact angle of pristine SiO₂/Si substrate is around 38.48°, while it drops rapidly to 6.04° after O₂ plasma treating for 10 min, similar to observations in previous reports (19). To compare the change in the physical surface due to O₂ plasma treatment, we also measured the contact angle of the surface treated by Ar plasma for the same duration (which gives similar surface roughness) (*SI Appendix*, Fig. S8). However, the Ar plasma-treated substrate shows a contact angle of about 36.22°, similar to that of the pristine SiO₂/Si. Thus, physical roughness is not the main contribution to the surface energy change.

To understand the difference in surface energies induced by different treatments, we conducted density functional theory (DFT) calculations. In our model, Ar plasma etching increases the number of dangling bonds on the surface of SiO₂/Si substrate, which serve as active sites to dissociate H₂O molecules in ambient environment, resulting in a hydroxylated surface (terminated by –OH group) (*SI Appendix*, Fig. S9). However, in the case of O₂ plasma, the oxygen bonds on the unsaturated surface site and yields an oxygen-rich surface. DFT calculations show that the binding energy of water with the oxygen-rich surface is over two times that of the Ar plasma-treated surface (Fig. 2C), consistent with the contact angle measurement in Fig. 2B. When considering the binding energy with Mo_3O_9 [the intermediate of MoO_{3-x} during the MoS₂ growth (29)], the oxygen-rich surface has ~1-eV higher binding energy than that of the hydroxylated surface (Fig. 2D). Combining the growth result (*SI Appendix*, Fig. S10) with DFT calculations, it is shown that the O₂ plasma-modified substrates have better wettability and higher binding energy to Mo_3O_9, which is beneficial for the monolayer growth of MoS₂. We experimentally verify this via results shown in Fig. 2E. On only supplying MoO₃ powder during the growth, Mo-containing species [MoO₂ as confirmed by Raman spectroscopy (30)] clearly preferred the O₂ plasma-treated regions over the nontreated regions. By adding PTAS, which is a hydrophilic salt and has preference for the patterned regions (23), Mo-based compounds may have higher adsorption within the patterned regions (as given by a stronger Raman signature after PTAS was added). Here, the presence of PTAS may increase the strength of surface adhesion between MoS₂ and SiO₂/Si, leading to the monolayer growth of MoS₂. Based on the different growth results in Fig. 2F, which show obvious growth enhancement under O₂ plasma and PTAS, we conclude that the combination of O₂ plasma treatment and PTAS exhibits a synergetic effect that promotes the optimized MoS₂ growth.

For the MoS₂ growth to distinguish the difference between the untreated and treated surfaces, we noted that the entrance timing of sulfur and its amount are critical, both of which will affect the concentration (or partial pressure) of sulfur in the gaseous phase. According to the Mo–O–S phase diagram (31), MoO₃ undergoes a two-step reaction in the chemical vapor deposition (CVD) growth of MoS₂ (32):

$$MoO_3(s) + x/2 S(g) \rightarrow MoO_{3-x}(g) + x/2 SO_2(g). \quad [1]$$

Next, $MoO_{3-x}(g)$ has two possible reaction paths:

$$MoO_{3-x}(g) + (7-x)/2 S(g) \rightarrow MoS_2(s) + (3-x)/2 SO_2(g) \quad [2.1]$$

$$MoO_{3-x}(g) + (1-x)/2 S(g) \rightarrow MoO_2(s) + (1-x)/2 SO_2(g). \quad [2.2]$$

Higher [S]/[Mo] ratio (here, [S] and [Mo] indicate the concentrations or partial pressures of S and Mo species) promotes
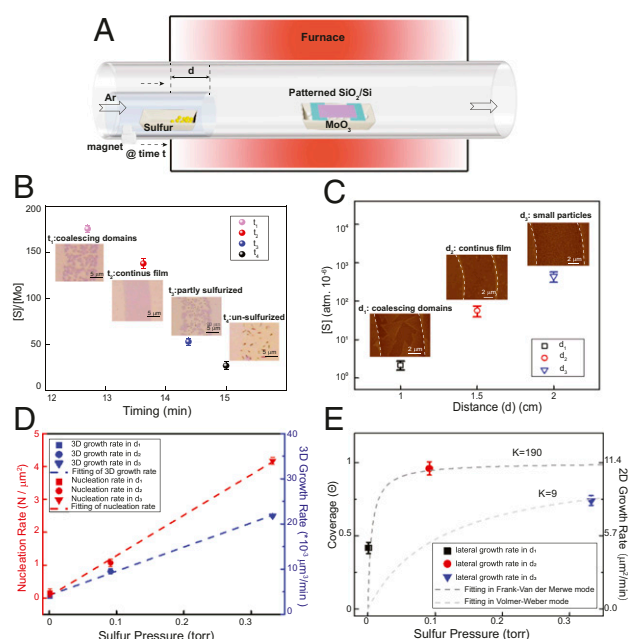
Fig. 3. The control of sulfur precursor during the patterned growth of monolayer MoS₂ nanostructures. (A) Schematic illustration of the modified CVD setup and the controlled process to synthesize patterned MoS₂ nanostructures. (B) The relationship between the entrance time of the sulfur precursor and the corresponding [S]/[Mo] ratio during the growth. (*Insets*) OM images of different growth results according to different entrance times of sulfur. (C) The relationship between the locations of the sulfur precursor (d) and the corresponding vapor pressures of sulfur. (*Insets*) AFM images of MoS₂ patterns grown as a result of different precursor locations. (D) The dependence of nucleation rate as the function of partial pressure of sulfur precursor (left y axis); the dependence of 3D growth rate as the function of partial pressure of sulfur precursor (right y axis). (E) The dependence of surface coverage as the function of partial pressure of sulfur precursor (left y axis); the dependence of 2D growth rate as the function of partial pressure of the sulfur precursor (right y axis).

the reaction in path [**2.1**], while lower [S]/[Mo] ratio tends to form MoO₂ as path [**2.2**]. To investigate the role of sulfur, we laid several patterned substrates as shown in *SI Appendix*, Fig. S11A (23). Presumably, the sulfur concentration decreases along the substrate as the distance away from the sulfur source increases, and the quality of the MoS₂ patterns in different regions of SiO₂/Si reflects the influence of sulfur concentration on the patterned growth. Instead of producing spatially distinguished MoS₂ patterns, higher sulfur concentration creates a continuous MoS₂ film across the entire surface (*SI Appendix*, Fig. S11B) (which means that there is no selective patterning by the substrate), while lower sulfur concentration produces discontinuous MoS₂ flakes (*SI Appendix*, Fig. S11E). Only under an appropriate concentration, we can produce patterned monolayer MoS₂ (*SI Appendix*, Fig. S11D). Therefore, we designed an improved CVD setup to control sulfur concentration during the growth. As shown in Fig. 3A, a small quartz tube is used to carry the sulfur boat, and a set of magnets is used to move the position of the sulfur boat. The sulfur powder is initially kept outside of the heating zone, and it is moved inside the heating zone during the ramping period when the MoO₃ precursor reaches a suitable temperature (*SI Appendix*, Fig. S12) (it takes 15 min for the center of the furnace to reach the growth temperature). We first found that the entrance timing of sulfur impacts the ratio of sulfur partial pressure to Mo partial pressure ([S]/[Mo]) due to the temperature difference at different entrance times (*SI Appendix*, Fig. S13 and Table S1). As shown in Fig. 3B, the [S]/[Mo] ratio has a negative correlation with the entrance timing of
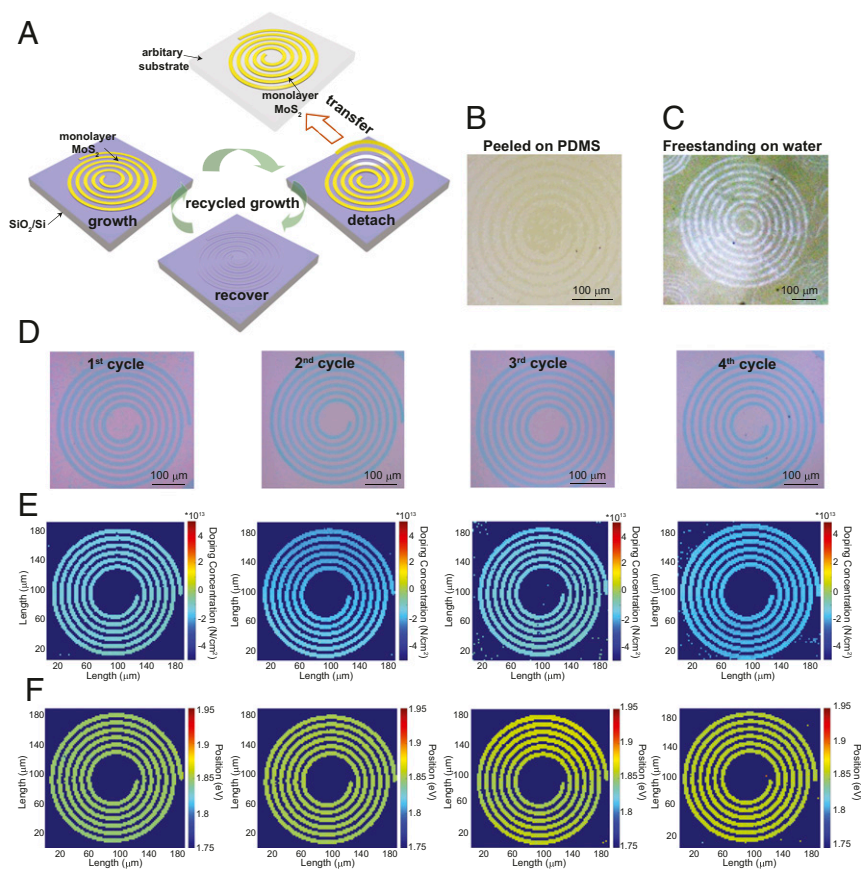
Fig. 4. Repeated growth of patterned monolayer MoS$_2$ nanostructures using the same template. (*A*) Schematic illustration of repeated growth procedures for directly grown MoS$_2$ patterns. (*B*) OM image of monolayer MoS$_2$ patterns peeled on PDMS. (*C*) OM image of monolayer MoS$_2$ structures freestanding on water without any additional support. (*D*) OM images of the monolayer MoS$_2$ spiral pattern after the first, second, third, and fourth growth cycles. (*E*) The carrier concentration mappings (via Raman) of the monolayer MoS$_2$ spiral after the first, second, third, and fourth growth cycles as given by *D*. (*F*) The photoluminescence position mappings (via PL spectrum) of the monolayer MoS$_2$ spiral after the first, second, third, and fourth growth cycles as given by *D*.

sulfur, which essentially dominates the degree of the sulfurization in the process. When sulfur is introduced relatively early (as shown in Fig. 3*B*) (at t_1 or t_2; before 14 min), the [S]/[Mo] is high enough to fully sulfurize MoO$_3$ into MoS$_2$. Nevertheless, to make continuous MoS$_2$ patterns, sufficient supply of molybdenum is also required (entering at t_2) compared with the lower supply of molybdenum at t_1. However, when sulfur enters at t_3, the [S]/[Mo] ratio decreases rapidly, resulting in only a part of MoO$_3$ turning into MoS$_2$. If sulfur enters at t_4 or later, only black MoO$_2$ particles are obtained on the substrate. Although MoO$_2$ can also be sulfurized into MoS$_2$ (33), the temperature needed (650 °C to 850 °C) is much higher than that in our growth. Additionally, the position where the sulfur boat is introduced (corresponding to the distance d in Fig. 3*C* and as illustrated in Fig. 3*A*) is another important factor of sulfur pressure, which therefore, determines the nucleation rate and growth rate of MoS$_2$. According to the temperature variation at different positions (i.e., different d values) (*SI Appendix*, Fig. S14), we semiquantitatively calculated the nucleation rate and the growth rate of the patterned growth of monolayer MoS$_2$ (*SI Appendix*, Table S2). In Fig. 3*C*, the [S] at d_1 is insufficient, leading to both low nucleation rate (Fig. 3*D*) and growth rate (Fig. 3*E*). While excess [S] at d_3 will increase the nucleation rate of MoS$_2$ dramatically, it also accelerates the MoS$_2$ nuclei growth rate in the vertical direction (corresponding to the 3D growth rate in Fig. 3*D*), which is significantly faster than that in the lateral direction (corresponding to 2D growth rate in Fig. 3*E*), leading to the formation of multilayer MoS$_2$ particles. If the sulfur partial

pressure is kept at an appropriate value (located at d_2), we could achieve medium nucleation rate and optimal growth rate in the lateral direction and obtain monolayer MoS$_2$ patterns.

As previously mentioned, electronic applications require patterned materials for device fabrication and integration. Nevertheless, previous methods to produce patterned 2D materials are limited by the single use of patterned substrates or etched materials. Therefore, developing a master–replica type of repeated growth of patterned TMD materials is highly attractive for 2D material device fabrication. Here, we have found that the prepatterned substrate can be repeatedly used through the noninvasive transfer of monolayer MoS$_2$ patterns. As shown in Fig. 4*A*, due to the weak interaction between the monolayer MoS$_2$ and the SiO$_2$/Si substrate, monolayer MoS$_2$ patterns can be easily detached (with preserved structural integrity) from the substrate by directly peeling with a polydimethylsiloxane (PDMS) stamp via dry transfer (Fig. 4*B*) or delaminating by water via wet transfer (Fig. 4*C* and *SI Appendix*, Figs. S15 and S16). Since the separation process is performed without any intermediate supporting layer or etchant, the released substrate with original patterns is recovered, which makes it possible for the next cycle of patterned growth. In our study, it was found that the patterned substrate can be reused at least four times without seeing signs of wear, and the quality of monolayer MoS$_2$ patterns is well preserved. Fig. 4*D* shows the OM images of MoS$_2$ spiral patterns grown from four "growth–detach" cycles on the same SiO$_2$/Si substrate after water delamination. It was found that the shape of the MoS$_2$ spiral in each cycle was well reserved and that the reflectance contrast was

uniform under the same illumination. The OM images of SiO$_2$/Si substrates before growth and after delamination (*SI Appendix*, Fig. S17) show that premade patterns on SiO$_2$/Si substrate are retained after this simple and clean transfer without visible damage and contamination. From our calculation, the O$_2$ plasma-treated substrates have lower binding energy with hydrocarbon species (the common contaminate in air) (*SI Appendix*, Fig. S18), which suggests a "contamination-resilient" feature of O-rich surfaces. This could be verified by our observation that the patterned substrates kept for several weeks are still as effective to patterned growth as freshly made. To evaluate the quality of the MoS$_2$ patterns grown by the recycled growth, we extracted strain (*SI Appendix*, Fig. S19) and carrier concentration maps (Fig. 4*E*) from the spatially resolved Raman analysis (34, 35) on the MoS$_2$ spirals grown each time using the same SiO$_2$/Si template. The strain and carrier concentration maps show a relatively small variation, indicating good consistency in the quality of MoS$_2$ patterns for different cycles. Moreover, the PL spectrum on monolayer MoS$_2$ from each cycle has few changes on the emission energy and FWHM (*SI Appendix*, Fig. S20). The photoluminescence position mappings (Fig. 4*F*) extracted from the PL spectrum analysis also demonstrate the preserved qualities. After delamination, these MoS$_2$ patterns floating on a water surface can be easily picked up onto arbitrary substrates, such as transparent quartz (*SI Appendix*, Fig. S21*A*) and flexible mica (*SI Appendix*, Fig. S21*B*), allowing for more efficient integration of complicated 2D device structures.

The key for repeated utilization of the same mask relies on the successful delamination (hence, on the quality of the monolayer MoS$_2$ patterns). If MoS$_2$ particles are grown, the patterns are difficult to delaminate by water, which will damage the surface integrity and reduce the lifetime of the master template. With well-controlled growth, successful transfer, and posttreated cleaning, it is anticipated that these prepatterned templates can be used many times. This additive manufacturing method paves the way for broad applications of 2D TMD nanostructures in modern electronics and optoelectronics with much simpler fabrication, lower cost, and higher efficiency.

Methods

To obtain patterned substrates for MoS$_2$ growth, photolithography and O$_2$ plasma treatment steps were first carried out as explained above. After removing the photoresist on the patterned SiO$_2$/Si wafer, the substrate was preannealed at 350 °C for 2 h with 300 standard cubic centimeters per minute (sccm) Ar and 100 sccm H$_2$ gases. Then, a piece of the patterned substrate was suspended between two SiO$_2$/Si substrates with predeposited PTAS (via solution dropping). All of these substrates were placed face down on a crucible containing MoO$_3$ precursor in a 1-inch quartz tube. This crucible was placed in the middle of the heating zone with another smaller tube containing the sulfur crucible upstream close to the cold end of the quartz tube. Before heating, the whole CVD system was purged with 1,000 sccm Ar (99.999% purity) for 3 min. Then, 20 sccm Ar was introduced into the system as a carrier gas. The growth system was heated to 625 °C for 15 min. At around 13 min, the sulfur crucible was pushed into the system by a magnet (as shown in Fig. 3*A*) at a distance of ~1.5 cm from the left edge of the furnace. The MoS$_2$ growth was carried out around 620 °C to 630 °C for 3 min under atmospheric pressure. The growth system was finally cooled down to room temperature quickly by opening the furnace and cooling using a fan.

1. Radisavljevic B, Kis A (2013) Mobility engineering and a metal-insulator transition in monolayer MoS$_2$. *Nat Mater* 12:815–820.
2. Bertolazzi S, Brivio J, Kis A (2011) Stretching and breaking of ultrathin MoS$_2$. *ACS Nano* 5:9703–9709.
3. Mak KF, McGill KL, Park J, McEuen PL (2014) Valleytronics. The valley hall effect in MoS$_2$ transistors. *Science* 344:1489–1492.
4. Wu W, et al. (2014) Piezoelectricity of single-atomic-layer MoS$_2$ for energy conversion and piezotronics. *Nature* 514:470–474.
5. Feng Q, et al. (2014) Semiconductors: Growth of large-area 2D MoS$_2$(1-x)Se$_{2x}$ semiconductor alloys (Adv. Mater. 17/2014). *Adv Mater* 26:2763.
6. Radisavljevic B, Radenovic A, Brivio J, Giacometti V, Kis A (2011) Single-layer MoS$_2$ transistors. *Nat Nanotechnol* 6:147–150.
7. Wang QH, Kalantar-Zadeh K, Kis A, Coleman JN, Strano MS (2012) Electronics and optoelectronics of two-dimensional transition metal dichalcogenides. *Nat Nanotechnol* 7:699–712.
8. Zheng W, et al. (2015) Patterning two-dimensional chalcogenide crystals of Bi$_2$Se$_3$ and In$_2$Se$_3$ and efficient photodetectors. *Nat Commun* 6:6972.
9. Yu Q, et al. (2011) Control and characterization of individual grains and grain boundaries in graphene grown by chemical vapour deposition. *Nat Mater* 10:443–449.
10. Zhou H, et al. (2013) Thickness-dependent patterning of MoS$_2$ sheets with well-oriented triangular pits by heating in air. *Nano Res* 6:703–711.
11. Mahjouri-Samani M, et al. (2015) Patterned arrays of lateral heterojunctions within monolayer two-dimensional semiconductors. *Nat Commun* 6:7749.
12. Xue Y, et al. (2016) Scalable production of a few-layer MoS$_2$/WS$_2$ vertical heterojunction array and its application for photodetectors. *ACS Nano* 10:573–580.
13. Park W, et al. (2014) Photoelectron spectroscopic imaging and device applications of large-area patternable single-layer MoS$_2$ synthesized by chemical vapor deposition. *ACS Nano* 8:4961–4968.
14. Cao L, et al. (2013) Direct laser-patterned micro-supercapacitors from paintable MoS$_2$ films. *Small* 9:2905–2910.
15. Kelly AG, et al. (2017) All-printed thin-film transistors from networks of liquid-exfoliated nanosheets. *Science* 356:69–73.
16. Han GH, et al. (2015) Seeded growth of highly crystalline molybdenum disulphide monolayers at controlled locations. *Nat Commun* 6:6128.
17. Song I, et al. (2014) Patternable large-scale molybdenium disulfide atomic layers grown by gold-assisted chemical vapor deposition. *Angew Chem Int Ed Engl* 53:1266–1269.
18. Kim H-J, Kim H, Yang S, Kwon J-Y (2017) Grains in selectively grown MoS thin films. *Small* 13:1702256.
19. Chen X, et al. (2016) Lithography-free plasma-induced patterned growth of MoS$_2$ and its heterojunction with graphene. *Nanoscale* 8:15181–15188.
20. Shyu TC, et al. (2015) A kirigami approach to engineering elasticity in nanocomposites through patterned defects. *Nat Mater* 14:785–789.
21. Lamoureux A, Lee K, Shlian M, Forrest SR, Shtein M (2015) Dynamic kirigami structures for integrated solar tracking. *Nat Commun* 6:8092.
22. Blees MK, et al. (2015) Graphene kirigami. *Nature* 524:204–207.
23. Ling X, et al. (2014) Role of the seeding promoter in MoS$_2$ growth by chemical vapor deposition. *Nano Lett* 14:464–472.
24. Ling X, et al. (2016) Parallel stitching of 2D materials. *Adv Mater* 28:2322–2329.
25. van der Zande AM, et al. (2013) Grains and grain boundaries in highly crystalline monolayer molybdenum disulphide. *Nat Mater* 12:554–561.
26. Kang K, et al. (2015) High-mobility three-atom-thick semiconducting films with wafer-scale homogeneity. *Nature* 520:656–660.
27. English CD, Shine G, Dorgan VE, Saraswat KC, Pop E (2016) Improved contacts to MoS$_2$ transistors by ultra-high vacuum metal deposition. *Nano Lett* 16:3824–3830.
28. ten Wolde PR, Frenkel D (1997) Enhancement of protein crystal nucleation by critical density fluctuations. *Science* 277:1975–1978.
29. Burns RP, DeMaria G, Drowart J, Grimley RT (1960) Mass spectrometric investigation of the sublimation of molybdenum dioxide. *J Chem Phys* 32:1363–1366.
30. Kumari L, et al. (2007) X-ray diffraction and Raman scattering studies on large-area array and nanobranched structure of 1D MoO$_2$ nanorods. *Nanotechnology* 18:115717.
31. Li H, Li Y, Aljarb A, Shi Y, Li L-J (2018) Epitaxial growth of two-dimensional layered transition-metal dichalcogenides: Growth mechanism, controllability, and scalability. *Chem Rev* 118:6134–6150.
32. Chhowalla M, et al. (2013) The chemistry of two-dimensional layered transition metal dichalcogenide nanosheets. *Nat Chem* 5:263–275.
33. Wang X, Feng H, Wu Y, Jiao L (2013) Controlled synthesis of highly crystalline MoS$_2$ flakes by chemical vapor deposition. *J Am Chem Soc* 135:5304–5307.
34. Michail A, Delikoukos N, Parthenios J, Galiotis C, Papagelis K (2016) Optical detection of strain and doping inhomogeneities in single layer MoS$_2$. *Appl Phys Lett* 108:173102.
35. Chae WH, Cain JD, Hanson ED, Murthy AA, Dravid VP (2017) Substrate-induced strain and charge doping in CVD-grown monolayer MoS$_2$. *Appl Phys Lett* 111:143106.

Supplementary Information

Additive Manufacturing of Patterned 2D Semiconductor through Recyclable Masked Growth

Yunfan Guo[1], Pin-Chun Shen[1], Cong Su[2], Ang-Yu Lu[1], Marek Hempel[1], Yimo Han[3], Qingqing Ji[1], Yuxuan Lin[1], Enzheng Shi[4], Elaine McVay[1], Letian Dou[4], David A. Muller[3], Tomás Palacios[2], Ju Li[2], Xi Ling[5*], Jing Kong[1*]

[1]Department of Electrical Engineering and Computer Science, Massachusetts Institute of Technology, Cambridge MA 02139, USA

[2]Department of Nuclear and Materials Science and Engineering, Massachusetts Institute of Technology, Cambridge MA 02139, USA

[3]School of Applied & Engineering Physics, Cornell University, Ithaca, New York 14850, USA

[4]Davidson School of Chemical Engineering, Purdue University, West Lafayette, IN 47907, USA

[5]Department of Chemistry, Division of Materials Science and Engineering, and The photonics Center, Boston University, Boston, MA 02215, USA

Supplementary Text

Characterization: AFM characterization was conducted on a Dimension 3100 instrument, from VEECO Instruments Inc. Raman and PL spectra were carried out on a Horiba Jobin-Yvon HR800 system and a Witec Alpha300-confocal Raman Microscope. The laser excitation wavelength for Raman and PL measurements were 532.5 nm. Laser power was about 0.1 mW. A 50X objective was used to focus the laser beam. For PL and Raman mapping, the scanning step sizes are 0.8 µm on a Horiba HR800 system, and 0.3 µm on a Witec Alpha 300-confocal Raman Microscope. The atomic structure of the sample was acquired by imaging using an aberration corrected Nion UltraSTEM100. The sample was baked in vacuum under 160°C for 8 hours before insertion into the microscope chamber. The electron acceleration voltage was kept at 60 kV during the operation to avoid the knock-on damage during imaging. The vacuum level during the experiments was kept under 3×10^{-9} mbar. The convergence angle of electron probe is 60 mrad and the collection angle of the high angle annular dark field (HAADF) is 70-200 mrad.

Device Fabrication and Measurement: Patterned monolayer MoS_2 nanostructures were first transferred onto 300 nm SiO_2/p+-Si substrates by the PMMA transfer method. E-beam lithography (EBL), e-beam evaporation followed by a lift-off process were used to deposit Ni/Au (30/20 nm) as electrodes. Since all devices are based on patterned monolayer MoS_2 nanostructures, there is no need to use oxygen plasma to isolate the channel area. The transport measurements were carried out under ambient environment at room temperature using a semiconductor parameter analyzer (Agilent 4155C) and a cryogenic probe station (Lakeshore).

FET Device based on patterned monolayer MoS₂. The linear output characteristics demonstrate that Ohmic-like contact is achieved at the interface. We extract the mobility of the MoS₂ FET using Equation (1).

$$\mu_{FE} = \frac{L_{ch}}{W_{ch}\, C_{ox}\, V_{ds}}\, \frac{dI_{ds}}{dV_{bg}} \tag{1}$$

where C_{ox} is the gate capacitance, L_{ch} (= 2 µm) and W_{ch} (= 10 µm) are channel length and width, respectively. The contact resistance (R_c) of our MoS₂ FETs was further extracted based on the transfer length method. Fig. 1*J* shows a linear fit to the total resistance normalized by channel width (R_{TOT}) versus L_{ch}, of which the vertical intercept yields the total contact resistance ($2R_c$). The carrier density n is estimated by a linear charge dependence on the gate voltage overdrive

$$n = \frac{C_{ox}}{q}(V_{bg} - V_T) \tag{2}$$

where V_T is the threshold voltage obtained by linear extrapolation at maximum trans-conductance for each channel (*SI Appendix,* Fig. S7b). We extract $R_c \approx 6.7$ kΩ.µm at room temperature for a carrier density n of about 1.8×10^{12} cm⁻².

First-principles calculation: First-principles calculation was performed using density functional theory (DFT) within the general gradient approximation (GGA), in the form of Perdew-Burke-Ernzerhof's exchange-correlation functional. The term for van der Waals correction is included in the Kohn-Sham energy as in the form of Grimme's DFT-D2 method. The energy cutoff for the plane wave basis set was chosen to be 350 eV for all the calculations. The code is implemented by the Vienna Ab-initio Simulation Package (VASP).
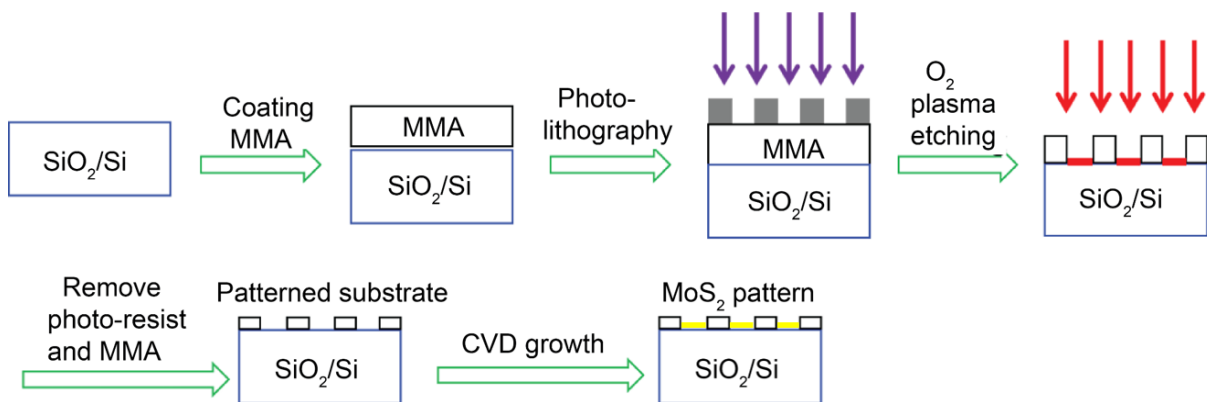
Figure S1. Schematic representation of procedure to directly grow MoS$_2$ patterns by modifying the growth substrate.
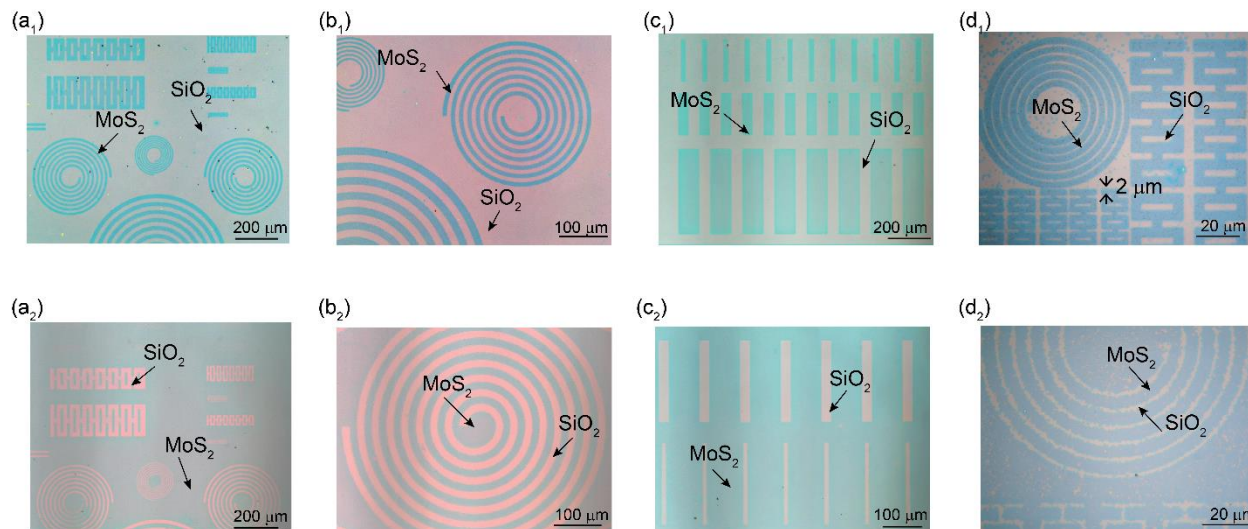
Figure S2. Optical microscope (OM) images of monolayer MoS$_2$ kirigami nanostructures and films. (a$_1$) Typical OM image of monolayer MoS$_2$ kirigami patterns on SiO$_2$/Si substrate. (a$_2$) Typical OM image of patterned monolayer MoS$_2$ film grows at the opposite locations when a negative photoresist was used for pattern in (a$_1$). (b$_1$-b$_2$) OM images of monolayer MoS$_2$ spiral patterns (b$_1$), and inverse MoS$_2$ spiral (b$_2$) on SiO$_2$/Si substrate. (c$_1$-c$_2$) OM images of monolayer

MoS$_2$ stripes in an 8×3 array (c$_1$), and inverse MoS$_2$ stripes (c$_2$) on SiO$_2$/Si. (d$_1$-d$_2$) OM images of monolayer MoS$_2$ spiral patterns (d$_1$), and inverse MoS$_2$ spiral pattern (d$_2$) on SiO$_2$/Si.
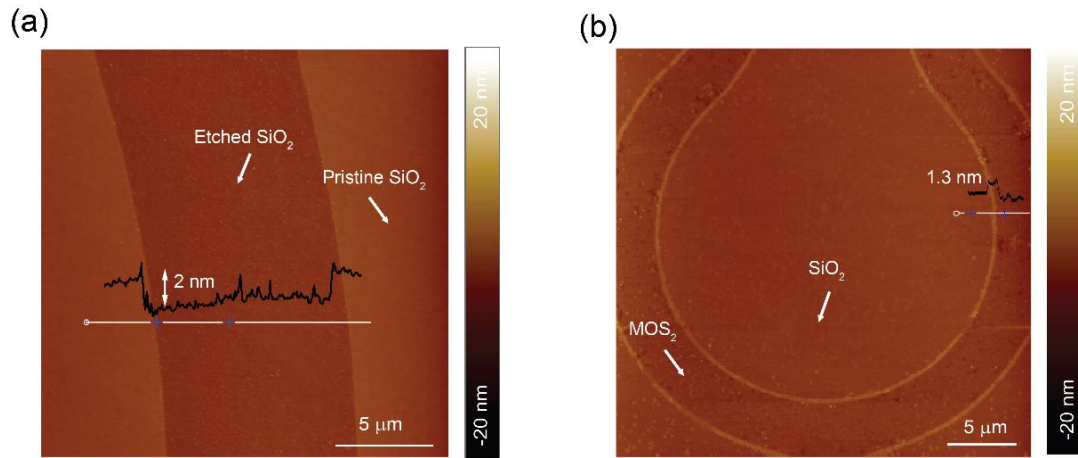
Figure S3. (a) AFM image and the corresponding height profile of the patterned SiO$_2$/Si substrate before MoS$_2$ growth. (b) AFM image and the corresponding height profile of a monolayer MoS$_2$ circular pattern grown on modified SiO$_2$/Si substrate.
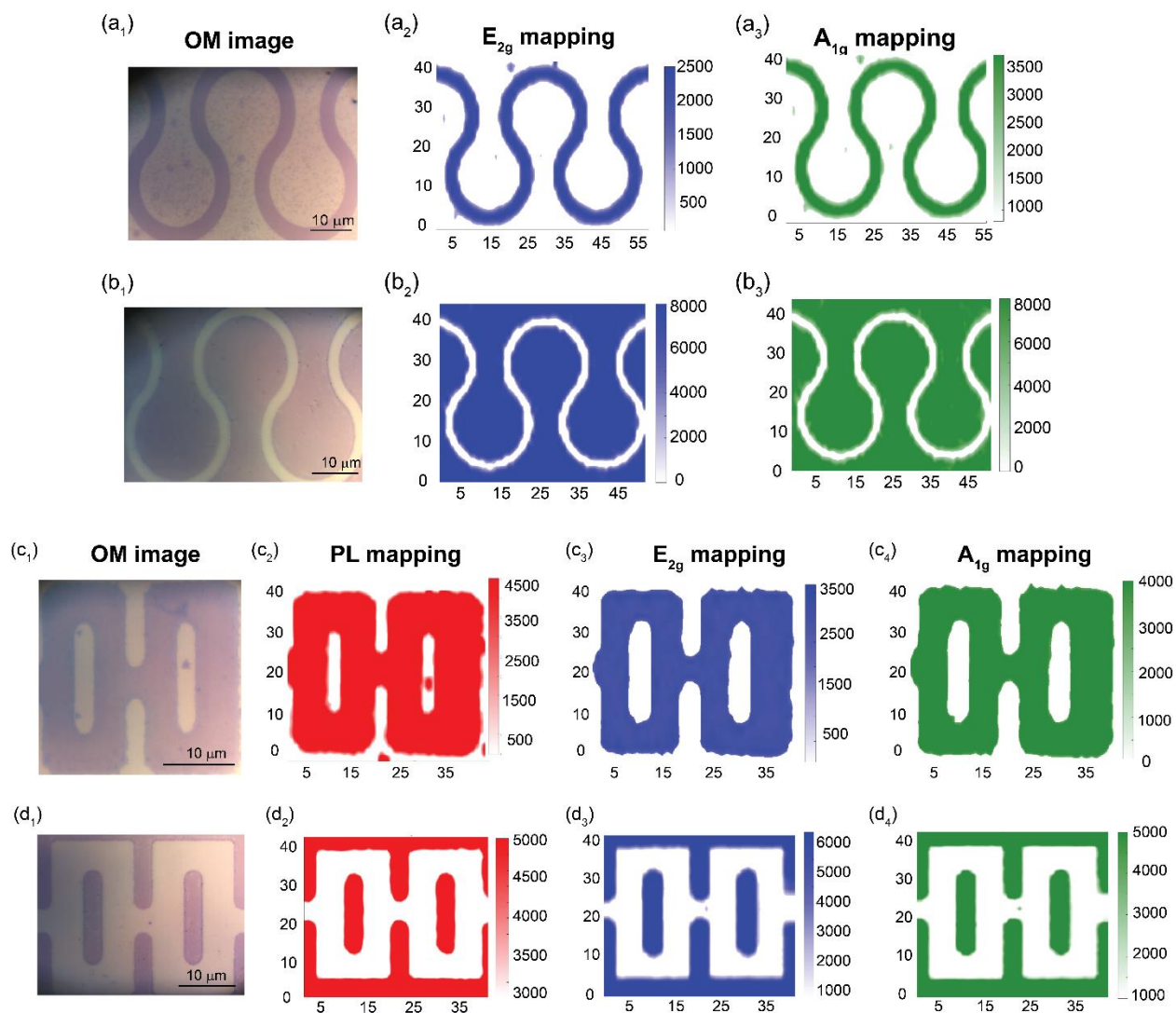
Figure S4. Optical microscope, Raman and PL spectra characterizations of the monolayer MoS$_2$ patterns. (a$_1$) OM image of a monolayer MoS$_2$ wave kirigami pattern. (a$_2$) The corresponding E$_{2g}$ Raman mapping image of MoS$_2$ pattern in (a$_1$). (a$_3$) The corresponding A$_{1g}$ Raman mapping image of MoS$_2$ pattern in (a$_1$). (b$_1$-b$_3$) OM image, E$_{2g}$ Raman mapping and A$_{1g}$ Raman mapping of a monolayer MoS$_2$ wave pattern. (c$_1$) OM image of a monolayer MoS$_2$ rectangle pattern. (c$_2$) The corresponding PL mapping of MoS$_2$ pattern in (c$_1$). (c$_3$, c$_4$) The corresponding Raman mappings (c$_3$ for E$_{2g}$ peak and c$_4$ for A$_{1g}$ peak) of MoS$_2$ pattern in (c$_1$). (d$_1$-d$_4$) OM image, PL mapping and Raman mappings of another monolayer MoS$_2$ pattern.
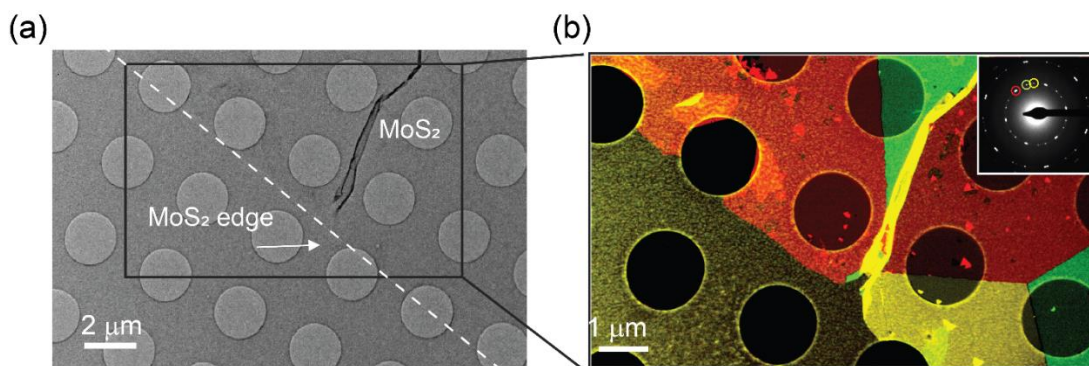
Figure S5. (a) Bright field TEM image of the edge of a monolayer MoS_2 pattern. (b) The corresponding dark field TEM image of the monolayer MoS_2 edge in (a), showing the grain size of the patterned region is greater than 5 μm. Inset: the diffraction image suggest this region is polycrystalline.
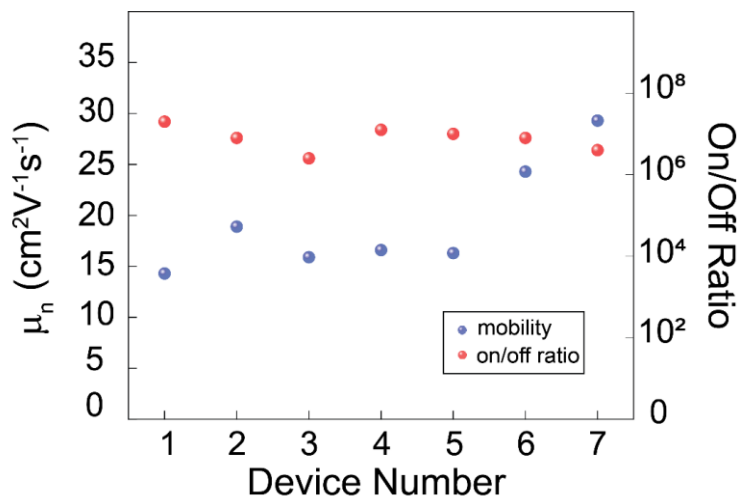
Figure S6. Electron mobility and on/off current ratio for 7 monolayer MoS_2 FETs measured in this work. All electrical measurements were carried out under ambient environment at room temperature.
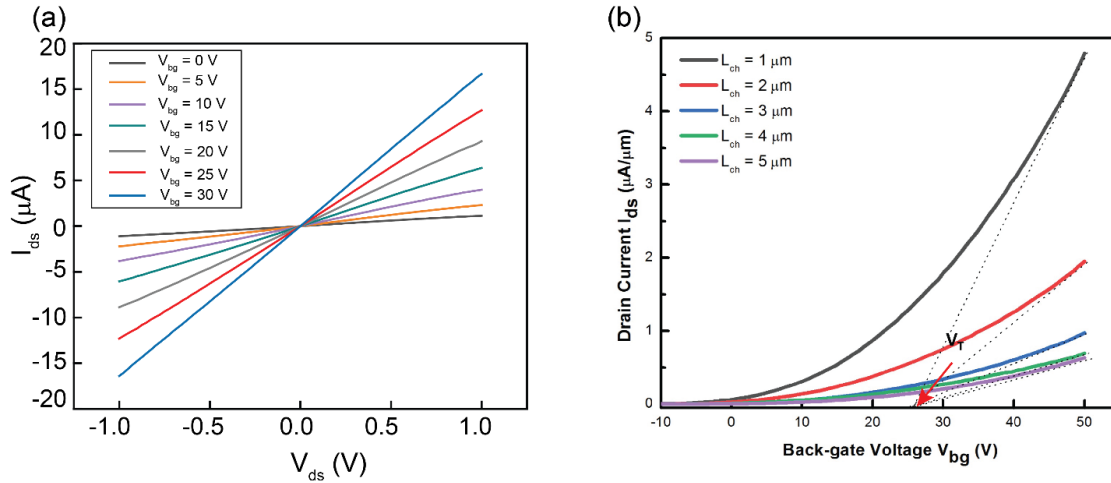
Figure S7. (a) Output *(I_{ds}–V_{ds})* characteristics of the same MoS$_2$ transistor with gate voltages from 0 to 30 V, the linear behavior suggesting Ohmic contacts between MoS$_2$ and Au electrodes. (b) I_{ds}–V_{bg} characteristics of five typical transistors fabricated on the directly grown MoS$_2$ patterns with different channel lengths, L (1, 2, 3, 4, and 5 μm).
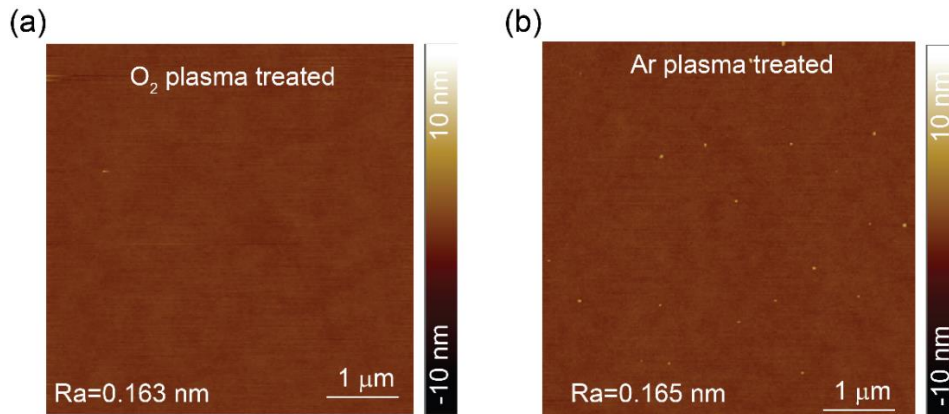
Figure S8. The comparison of surface roughness for O$_2$ plasma and Ar plasma treated SiO$_2$/Si substrates. (a) AFM height of O$_2$ plasma treated SiO$_2$/Si substrate. (b) AFM height of Ar plasma treated SiO$_2$/Si substrate.
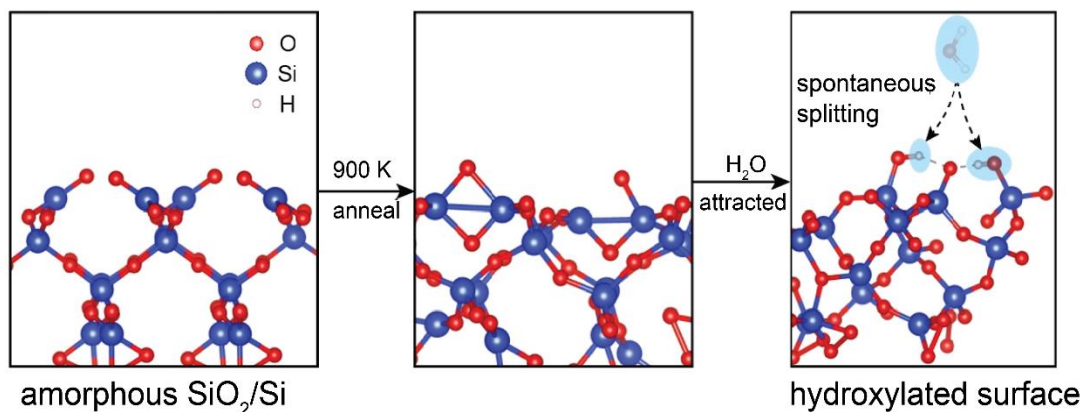
Figure S9. The hydroxylation process for amorphous SiO_2/Si substrates.
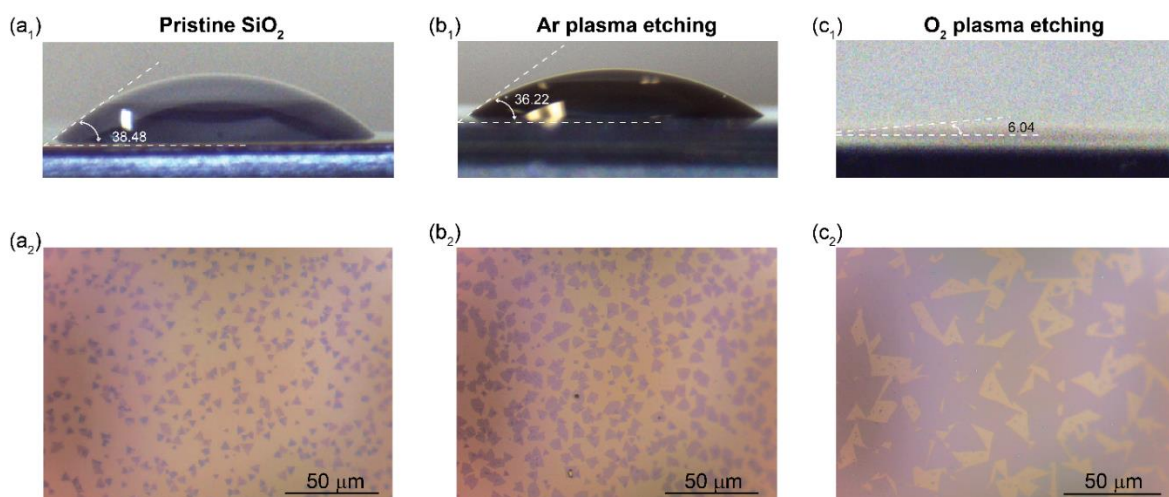
Figure S10. The contact angles of SiO_2/Si treated by different methods, and CVD growth results of MoS_2 flakes grown on corresponding treated surfaces. (a1, a2) contact angle for pristine SiO_2/Si substrate (a1), and the OM image of MoS_2 grown on pristine SiO_2/Si (a2). (b1, b2) contact angle for Ar plasma treated SiO_2/Si substrate (b1), and the OM image of MoS_2 grown on Ar plasma treated SiO_2/Si (b2). (c1, c2) contact angle for O_2 plasma treated SiO_2/Si substrate (c1), and the OM image of MoS_2 grown on O_2 plasma treated SiO_2/Si (c2). The results here indicate that

substrates with better wettability (thus higher surface energies) are more beneficial for the growth of monolayer MoS_2.
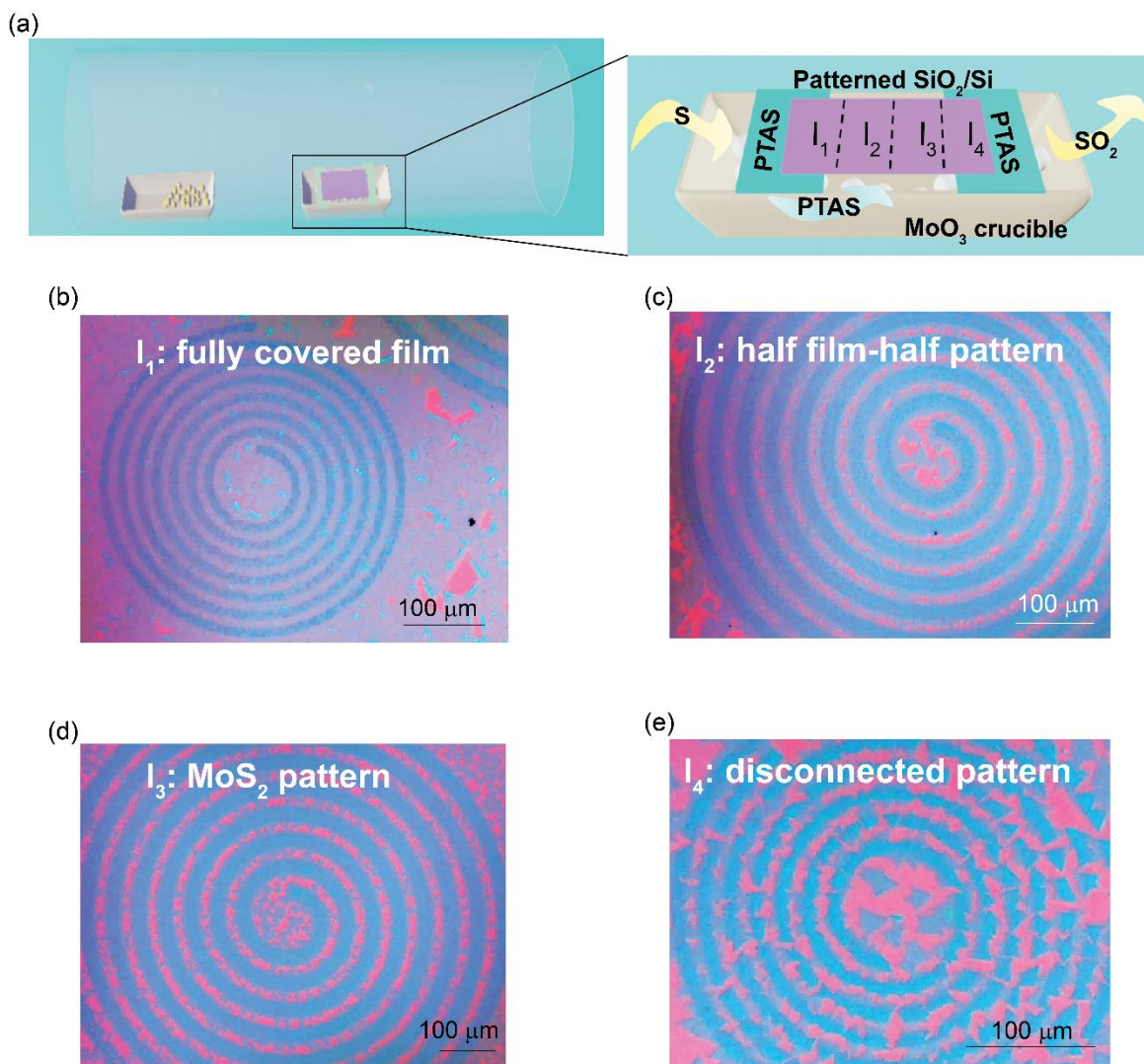
Figure S11. (a) Schematic illustration and the enlarged feature of the MoO_3 crucible covered by patterned SiO_2/Si substrate in a typical CVD growth system. (b-e) OM images of MoS_2 patterns grown on different regions (l_1-l_4) with different sulfur concentration. The sulfur concentration decreases from region l_1 in (b) to region l_4 in (e).
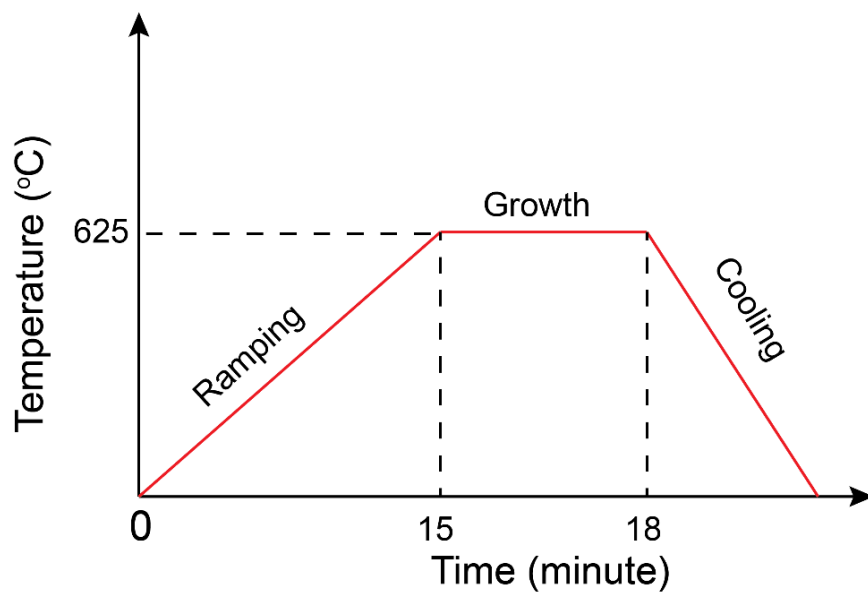
Figure S12. The temperature profile of the MoS$_2$ growth process used for this work.
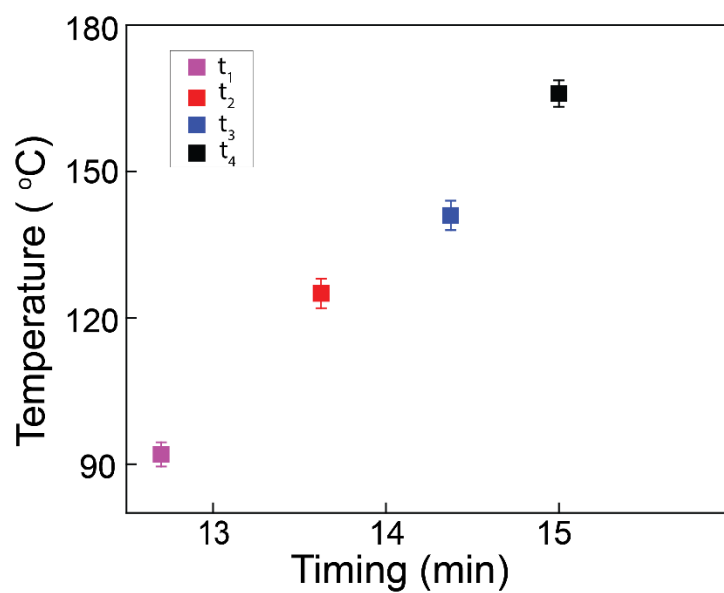
Figure S13. The relationship between the entrance timing of the sulfur precursor and the heating temperature at the corresponding location.

Table S1. Chart of the temperatures and partial pressures of sulfur and MoO_3, respectively, at different entrance timing of sulfur precursor, (formulas see in ref. 1 and 2). The distance between the left edge of furnace and the front of sulfur boat is around 1.5 cm, corresponding to "d_2" in Figure. 3C and Figure S14.

|	t_1	t_2	t_3	t_4
T_{MoO3}	520 °C	570 °C	600 °C	625 °C
P_{MoO3}	0.135×10^{-7} atm.	4.8295×10^{-7} atm.	33.8×10^{-7} atm.	154.94×10^{-7} atm.
T_{Sulfur}	92 °C	125 °C	141 °C	166 °C
P_{Sulfur}	2.3×10^{-6} atm.	6.8×10^{-5} atm.	1.4×10^{-4} atm.	4.28×10^{-4} atm.
[S]/[MoO₃]	175.37	137.79	53	27
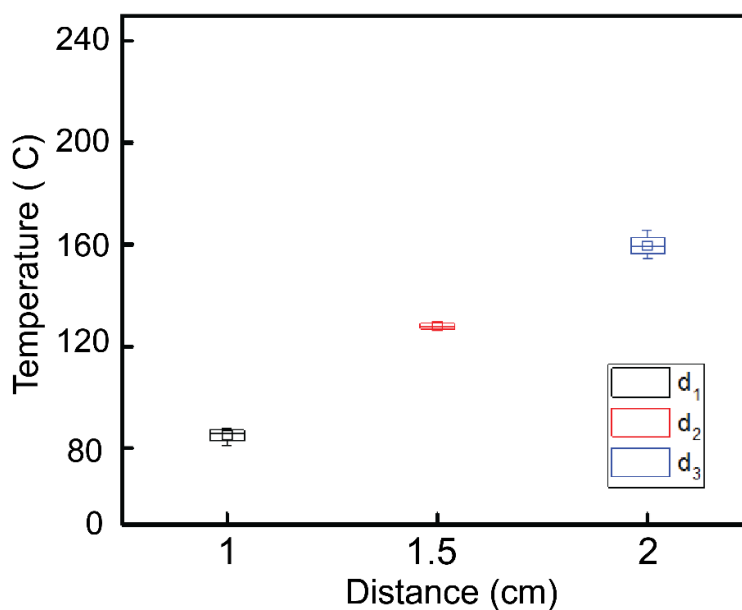
Figure S14. The relationship between the locations of the sulfur boat and the corresponding temperatures.

Table S2. The temperature, partial pressure of sulfur precursor, nucleation rate ($\dot{N}$) and growth rate ($\dot{G}$) in three dimensional (3D) and 2D of MoS_2 patterns at different offset locations of the sulfur boat. The nucleation rate and growth rate were semi-quantitatively calculated based on the following formulas[3], respectively: $\dot{N} = 2\pi r^* a_0 sin\theta \frac{PN_A}{(2\pi MRT)^{1/2}} n_s exp(\frac{E_{des}-E_S-\Delta G^*}{k_B T})$; $\dot{G} = \frac{MP\dot{V}}{k_B T \rho A}$ (in 3D); $\dot{G} = \frac{AMoS2/Atot}{tgrowth} \cdot h_{MoS2} \cdot A_{tot}$ (in 2D)
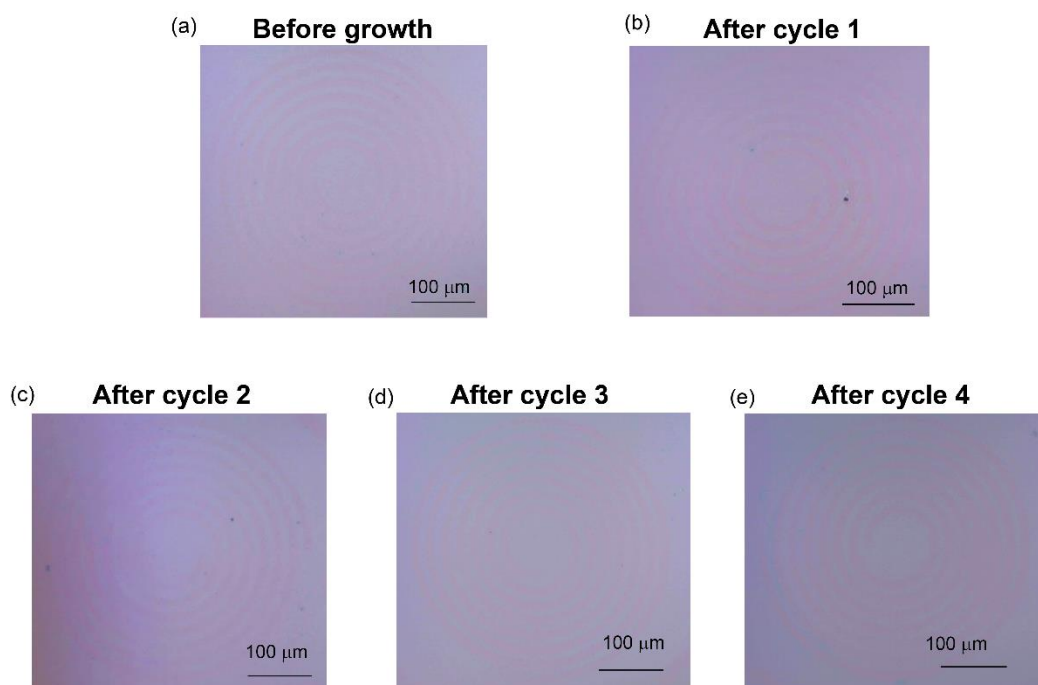
	d_1 (1 cm)	d_2 (1.5 cm)	d_3 (2 cm)
T_{Sulfur}	85	125	160
(P_{Sulfur})	8.968×10^{-4} tor	9.12×10^{-2} tor	0.332 tor
$\dot{N}$	0.05 ± 0.02	0.8125 ± 0.08	2.5 ± 0.05
(3D) $\dot{G}$	4.75 ± 0.9	11.4 ± 0.8	34 ± 0.8
(2D) $\dot{G}$	0.416 ± 0.038	0.96 ± 0.045	0.74 ± 0.033
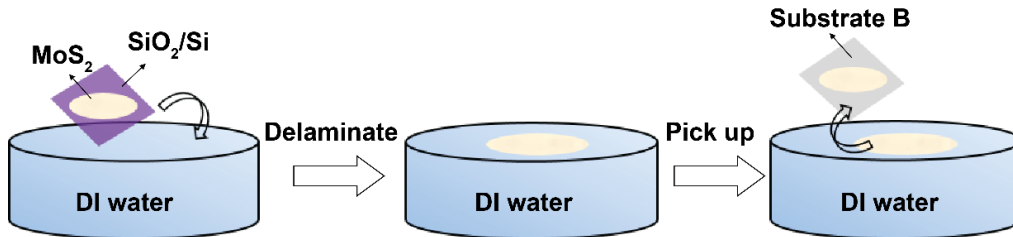
Figure S15. Schematic representation of water delamination procedures for the directly grown MoS_2 patterns.

(a) **Floating on water**   (b) **Free-standing on water**

100 μm

500 μm
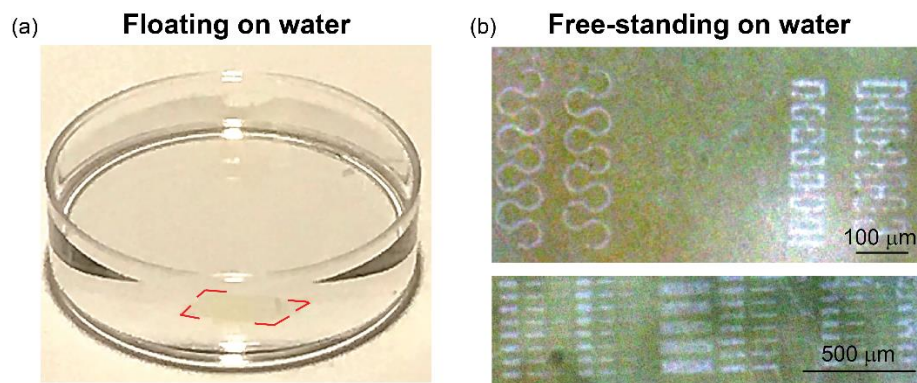
Figure S16. (a) Photograph for monolayer patterned MoS$_2$ film floating on the surface of water. (b) OM images of monolayer MoS$_2$ kirigami structures freestanding on a water surface without any additional support.


(a) **Before growth**   (b) **After cycle 1**

100 μm   100 μm

(c) **After cycle 2**   (d) **After cycle 3**   (e) **After cycle 4**

100 μm   100 μm   100 μm

Figure S17. Water delaminating transfer and recycled growth of patterned MoS$_2$ nanostructures. (a) OM image of the patterned SiO$_2$/Si substrate before growth. (b-e) OM images

of patterned SiO$_2$/Si substrates after the first through fourth cycles of the water delaminating transfer.
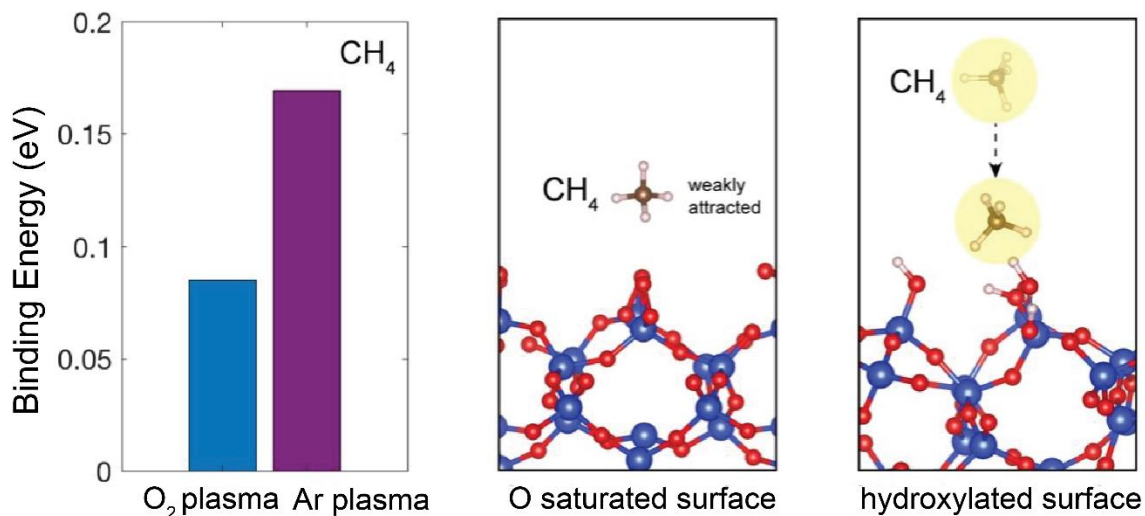
Figure S18. DFT calculation for the binding energy between amorphous carbon (to simplify the calculation, we use CH$_4$, which contains only one carbon atom to stand for amorphous carbon) and the growth substrates treated by O$_2$ plasma and Ar plasma. The O saturated surface is only weakly attractive to CH$_4$ molecule, while the hydroxylated surface has a higher binding energy for CH$_4$, indicating the O saturated surface condition is relatively more stable when compared with hydroxylated surface in air.
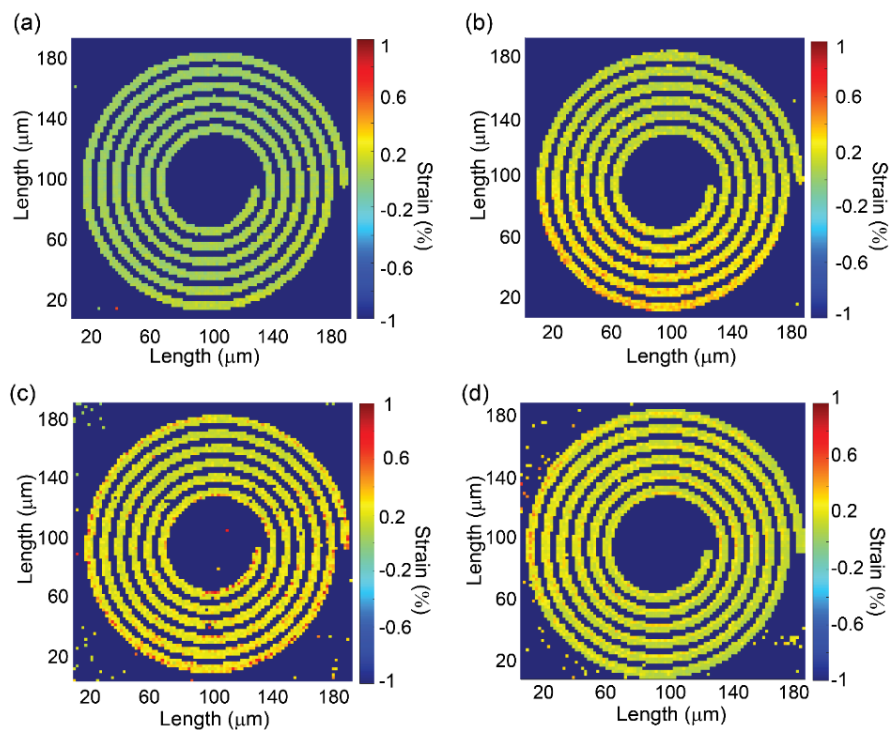
Figure S19. The strain mappings (via Raman) of monolayer MoS$_2$ spirals after the first through fourth growth cycles.
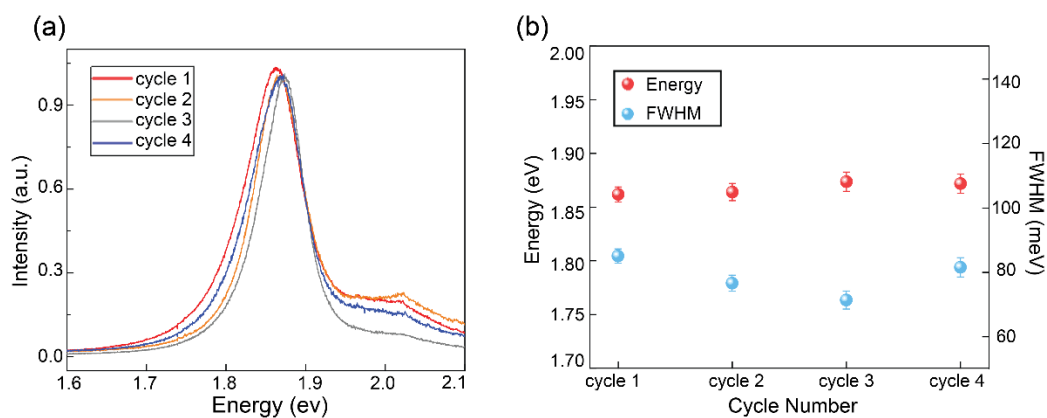
Figure S20. PL characterizations for repeated growth of monolayer MoS$_2$ patterns. (a) Normalized PL spectra collected on MoS$_2$ spiral structures in Fig. 4*F*. (b) The comparison for PL

peak energy and FWHM among samples grown in each cycle. Red dots correspond to the PL peak energy, and blue dots correspond to the FWHM of the PL.

(a)   (b)
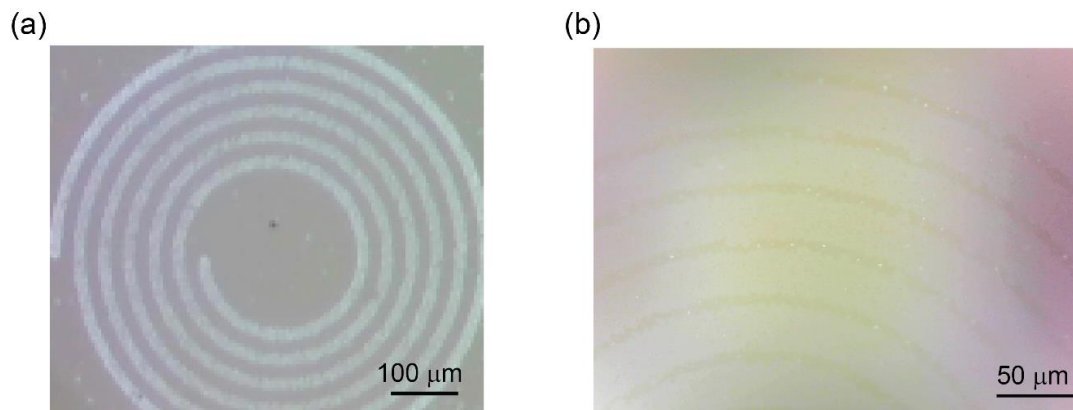
Figure S21. (a) OM image of a monolayer MoS_2 spiral spring transferred to a transparent quartz substrate. (b) OM image for monolayer MoS_2 spiral spring transferred to a transparent mica substrate.

Reference:

1. West, W. A. & Menzies, A. W. C. The Vapor Pressures of Sulphur between 100° and 550° with related Thermal Data. *J. Phys. Chem.* **33,** 1880–1892 (1928).

2. Blackburn, Paul E., Michael Hoch & Johnston Herrick L. The vaporization of molybdenum and tungsten oxides. *J. Phys. Chem.* **62**, 769–773 (1958).

3. Ohring, M. *Materials Science of Thin Films*. (Elsevier, 2001).